ELSEVIER

Volume 180, Number 7, July 2007

JOURNAL OF SOLID STATE CHEMISTRY

www.elsevier.com/locate/jssc

CONTENTS

Abstracted/indexed in BioEngineering Abstracts, Chemical Abstracts, Coal Abstracts, Current Contents/Physics, Chemical, & Earth Sciences, Engineering Index, Research Alert, SCISEARCH, Science Abstracts, and Science Citation Index. Also covered in the abstract and citation database SCOPUS®. Full text available on ScienceDirect®.

Regular Articles

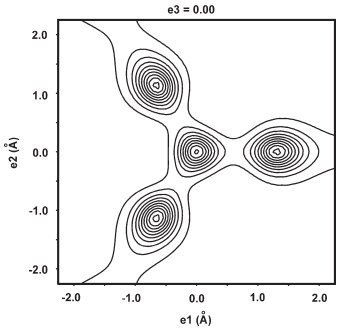

The 2D contour plot of the carbonate ion calculated by MEM in $Ba_7Ru_4Br_{1.46}(CO_3)_{0.27}O_{15}$.

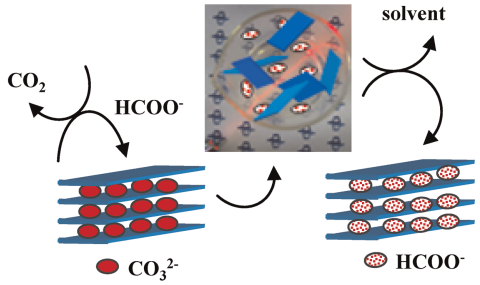

Hydrotalcite suspended in 1:1 (v/v) *N*,*N*-dimethylformamide–ethanol solvent mixture, at ambient temperature, undergoes decarbonation and exfoliation. The process is promoted by DMF hydrolysis. Restacking of LDH layers is achieved by evaporating the solvent.

Regular Articles—Continued

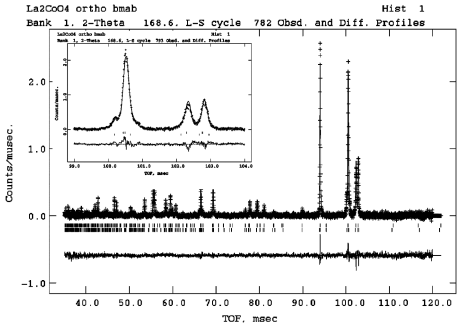

Two phase fit for $La_2CoO_{4+\delta}$ recorded at 150 °C showing the peak splitting of the two orthorhombic phases. Both phases transform to the tetragonal modification at elevated temperatures.

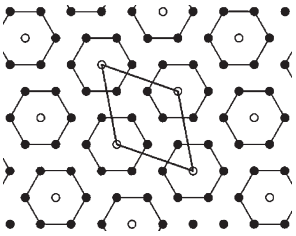

Schematic gallium vacancy distribution within a Ga-plane in wurtzite-type gallium oxynitride prepared via a citrate precursor route. Closed and open circles represent gallium and its vacancy sites, respectively. This is the most probable case among various kinds of statistical vacancy distribution, where Ga/vacancy = 6/1 in atomic ratio. About 10 at% Li^+ could be doped to the gallium oxynitride by substituting Ga^{3+}. Well-crystallized new oxynitride, $Li_2Ga_3NO_4$, isostructural with h-GaN, was also obtained in the preparation with $Li/Ga \geqslant 1$.

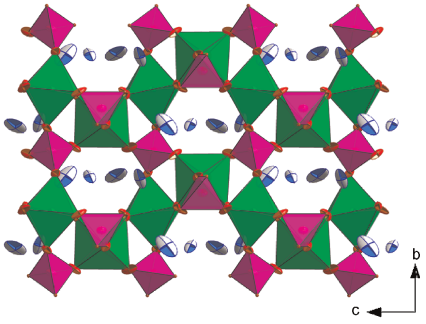

Chain-structure fragment of $KM^{II}_{0.33}Nb_{0.67}PO_5$ (M^{II}—Mn, Co) viewed along the [100] direction. K atoms are located in the cavities of anionic framework.

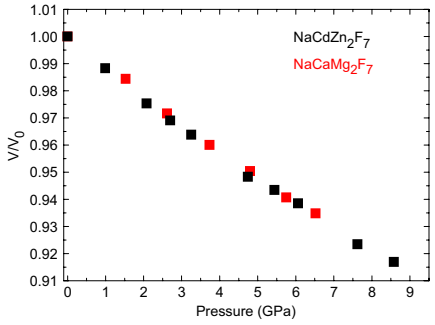

Pressure dependence of reduced unit-cell volumes in $NaCdZn_2F_7$ (black symbols) and $NaCaMg_2F_7$ (red symbols).

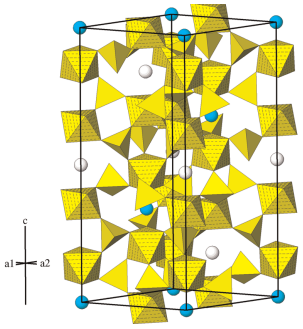

Polyhedral view down [110] of the $Fe_{0.50}Ti_2(PO_4)_3$ structure ([TiO_6] octahedra are shown with light shading, [PO_4] tetrahedra with dark shading, Fe/□ as circles).

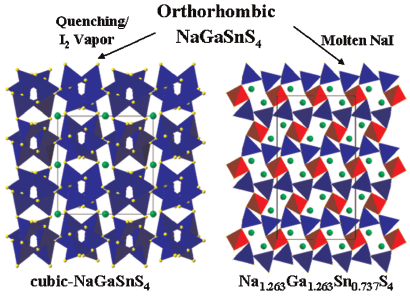

Orthorhombic-$NaGaSnS_4$ transforms, on quenching or during iodine vapor transport, to thermodynamically stable cubic form of $AGaSnS_4$ (A = Na, K, Rb, Cs, Tl) compounds and decomposes, in molten NaI, to isostructural $Na_{1.263}Ga_{1.263}Sn_{0.737}S_4$.

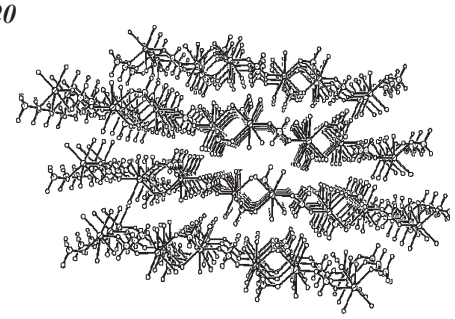

Two new lanthanum sulfates $DySO_4(OH)$ **1** and $Eu_2(SO_4)_3(H_2O)_8$ **2** have been hydrothermally synthesized. The colorless crystals were characterized by IR, TGA, ICP and XRD. The structure was determined by single-crystal X-ray diffraction. It displays a three dimensional framework, based on the novel Dy-O chains connected by the sulfate groups through helical chains.

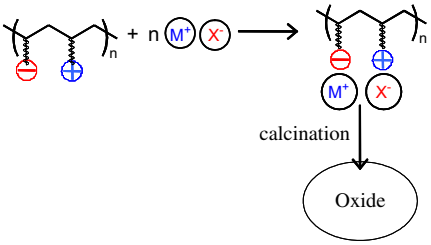

An alternative route based on hybrid organic–inorganic materials was implemented to synthesise Nb–Ta, Nb–Mo and Nb–V oxides. The hybrid materials were prepared by incorporation of inorganic salts based on Nb^V, Ta^V, V^V and Mo^{VI} in an organic polymer bearing cationic as well as anionic moieties. A thermal treatment of these hybrid blends has allowed the formation of multimetallic oxides.

Continued

An in situ time-of-flight neutron powder diffraction study of the humidity-induced phase transition in sodium monothiophosphate

Nathan J. Takas and Jennifer A. Aitken

Page 2034

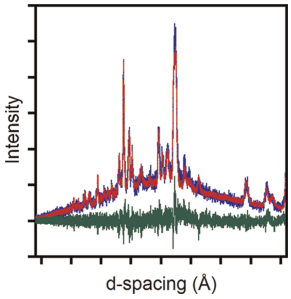

Anhydrous β-Na_3PO_3S has been observed to convert to anhydrous α-Na_3PO_3S upon exposure to a humid atmosphere. In situ neutron powder diffraction was used to monitor the transition. A whole pattern fitting method was used to determine the phase composition, as a function of time. The data were evaluated using several solid-state kinetic models.

A large series of isotypic Mo(V) diphosphates with a tunnel structure: From $A(MoO)_{10}(P_2O_7)_8$ with A = Ba, Sr, Ca, Cd, Pb to $A(MoO)_5(P_2O_7)_4$ with A = Ag, Li, Na, K

André Leclaire, Vincent Caignaert and Bernard Raveau

Page 2044

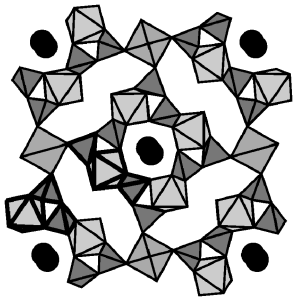

The structure of $Pb(MoO)_{10}(P_2O_7)_8$ viewed along b with the Pb ions in the octagonal tunnels.

Crystal structures of the $La_3AgSnSe_7$ and $R_3Ag_{1-\delta}SnS_7$ (R = La, Ce; δ = 0.18–0.19) compounds

M. Daszkiewicz, L.D. Gulay, A. Pietraszko and V.Ya. Shemet

Page 2053

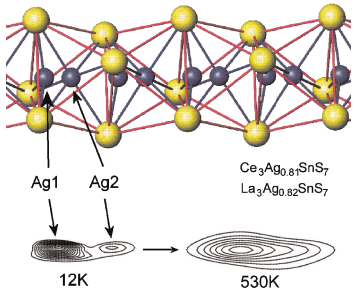

In the $R_3Ag_{1-\delta}SnS_7$ (R = La, Ce; δ = 0.18–0.19(1)) compounds high mobility of the Ag atom was found at different temperature conditions (12–530 K). The pseudopotentials determined through the Ag atoms shows relatively low barrier between two nearest positions which decreases when temperature rises.

Synthesis and characterization of layered zinc hydroxychlorides

Hidekazu Tanaka, Akiko Fujioka, Aya Futoyu, Kazuhiko Kandori and Tatsuo Ishikawa

Page 2061

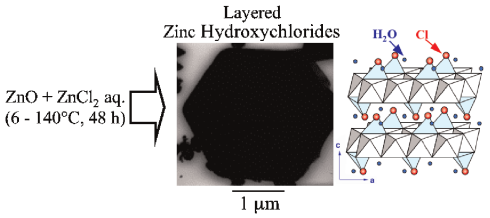

Layered zinc hydroxychlorides ($Zn_5(OH)_8Cl_2 \cdot H_2O$: ZHC) were synthesized from ZnO nano-particles aged with aqueous $ZnCl_2$ solutions at different temperatures ranging from 6 to 140 °C for 48 h. The ZHC particles obtained were hexagonal plate particles with sizes ranging from 1 to 3 μm.

Synthesis, characterization, photoluminescence and EPR investigations of Mn doped $MgAl_2O_4$ phosphors

Vijay Singh, R.P.S. Chakradhar, J.L. Rao and Dong-Kuk Kim

Page 2067

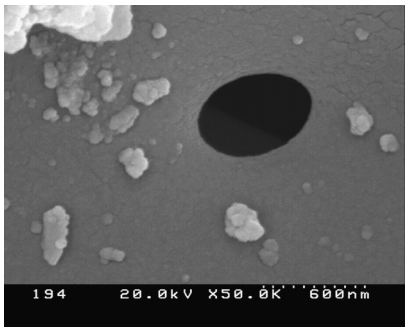

$MgAl_2O_4$:Mn phosphors have been prepared at 500 °C by combustion route and are well characterized by PXRD, SEM and FTIR. Photoluminescence studies showed green/red emission indicating two independent luminescence channels in this phosphor. EPR spectrum exhibits allowed and forbidden hyperfine structure at g = 2.003. From EPR spectra the spin-Hamiltonian parameters have been evaluated and discussed.

Neutron powder diffraction experiments on the layered triangular-lattice antiferromagnets $RbFe(MoO_4)_2$ and $CsFe(SO_4)_2$

Toshiya Inami

Page 2075

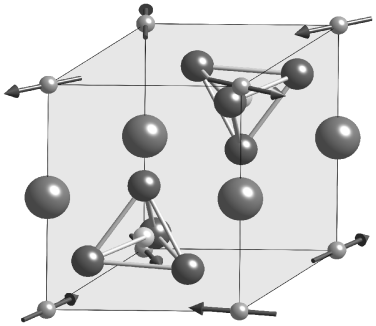

Crystal and magnetic structure of $RbFe(MoO_4)_2$.

Vapor-thermal preparation of highly crystallized TiO_2 powder and its photocatalytic activity
Yaorong Su, Jiaguo Yu and Jun Lin
Page 2080

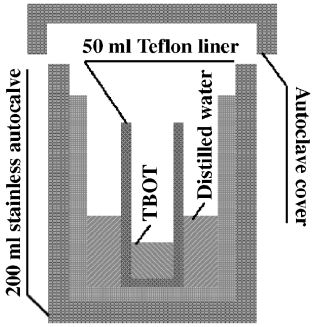

Nanocrystalline anatase TiO_2 powder photocatalysts with a very high photocatalytic activity were synthesized by a vapor-thermal method using tetrabutyl titanate as precursor at a temperature range from 120 to 200 °C.

Synthesis, crystal structures, magnetic and electric transport properties of $Eu_{11}InSb_9$ and $Yb_{11}InSb_9$
Sheng-qing Xia, Jonathan Hullmann, Svilen Bobev, Arif Ozbay, Edmund R. Nowak and Veronika Fritsch
Page 2088

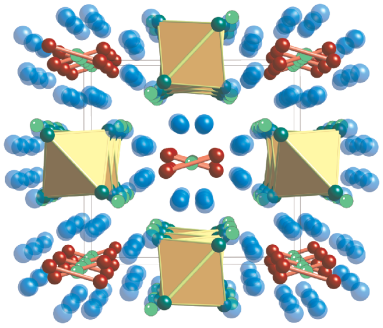

Reported are the synthesis, the structure and the magnetic and electronic properties of two new rare-earth Zintl phases, $Eu_{11}InSb_9$ and $Yb_{11}InSb_9$. The close relationships between these structures and those of the monoclinic α-$Ca_{21}Mn_4Sb_{18}$ and $Ca_{21}Mn_4Bi_{18}$ are also discussed.

Hydrothermal synthesis of nickel hydroxide nanostructures in mixed solvents of water and alcohol
Li-Xia Yang, Ying-Jie Zhu, Hua Tong, Zhen-Hua Liang, Liang Li and Ling Zhang
Page 2095

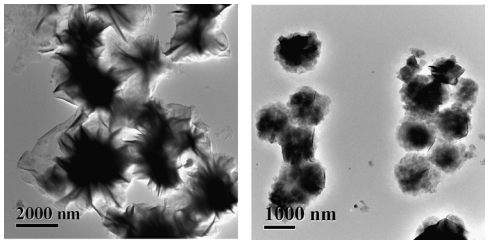

Nickel hydroxide nanosheets and flowers have been hydrothermally synthesized using $Ni(CH_3COO)_2 \cdot 4H_2O$ in mixed solvents of ethylene glycol (EG) or ethanol and deionized water at 200 °C for different reaction time. Porous nickel oxide nanosheets are obtained by heating nickel hydroxide nanosheets in air at 400 °C.

Synthesis of new mixed valence compounds $MV^{5+}V_2^{4+}O_7(M = NH_4, K)$: Crystal structure of $NH_4V_3O_7$ and electrical properties of KV_3O_7
J.C. Trombe, O. Szajwaj, Ph. Salles and Jean Galy
Page 2102

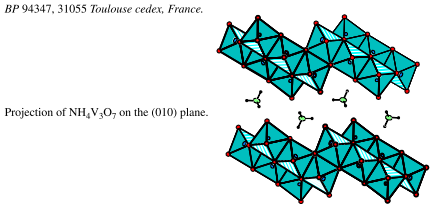

Projection of $NH_4V_3O_7$ on the (0 1 0) plane.

$Na(H_3NCH_2CH_2NH_3)_{0.5}[Co(C_2O_4)(HPO_4)]$: A novel phosphoxalate open-framework compound incorporating both an alkali cation and an organic template in the structural tunnels
Tao Huang, Britt A. Vanchura, Yongkui Shan and Songping D. Huang
Page 2110

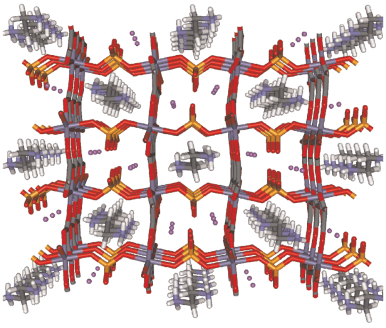

View along *a* of the structure of $Na(H_3NCH_2CH_2NH_3)_{0.5}[Co(C_2O_4)(HPO_4)]$ exhibiting 3D tunnels created and occupied by the Na^+ and $H_3NCH_2CH_2NH_3^{2+}$ cations.

Synthesis of a novel chromium-phosphate built up with unprecedented $[CR_9P_{12}O_{58}H_{12}]^{17-}$ clusters under hydrothermal conditions
Wei Liu, Ding-Bang Xiong, Xin-Xin Yang and Jing-Tai Zhao
Page 2116

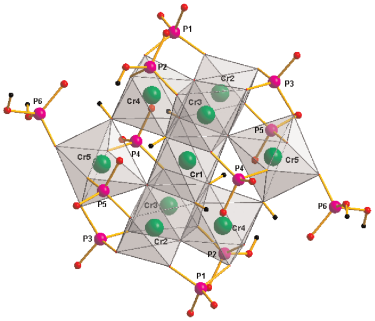

Polyhedral representation of the oxo-chromium core in compound **1**, showing the bridging function of phosphate groups around the octahedral chromium core (CrO_6 octahedron, grey and transparent; Cr, green sphere; P, pink sphere; O, red sphere; H, small black sphere).

Continued

Fe(II)-induced transformation from ferrihydrite to lepidocrocite and goethite

Hui Liu, Ping Li, Meiying Zhu, Yu Wei and Yuhan Sun

Page 2121

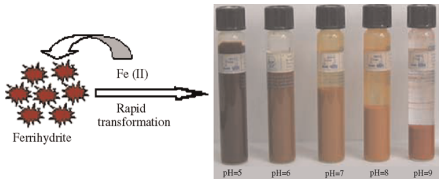

Fe(II)-adsorbed ferrihydrite can rapidly transform into lepidocrocite or/and goethite or/and hematite. Which product dominates depends on the transformation conditions of ferrihydrite such as temperature, pH, reaction time, etc. In the current system, there exist two transformation mechanisms. One is dissolution/reprecipitation and the other is solid-state transformation. The transformation mechanisms from Fe(II)-adsorbed ferrihydrite to lepidocrocite and goethite were investigated.

Syntheses, structure, magnetism, and optical properties of the interlanthanide sulfides δ-$Ln_{2-x}Lu_xS_3$ (Ln = Ce, Pr, Nd)

Geng Bang Jin, Eun Sang Choi, Robert P. Guertin, James S. Brooks, Travis H. Bray, Corwin H. Booth and Thomas E. Albrecht-Schmitt

Page 2129

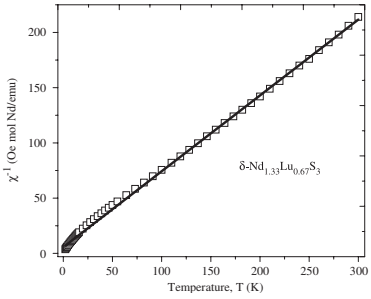

Inverse molar neodymium magnetic susceptibility vs. T for δ-$Nd_{1.33}Lu_{0.67}S_3$ under an applied magnetic field of $0.1T$ between 2 and 300 K. The straight line represents the fit to Curie–Weiss law in the range of 100–300 K.

Synthesis, characterization of TiO_2 nanotubes-supported MS (TiO_2NTs@MS, M = Cd, Zn) and their photocatalytic activity

Hong Li, Baolin Zhu, Yunfeng Feng, Shurong Wang, Shoumin Zhang and Weiping Huang

Page 2136

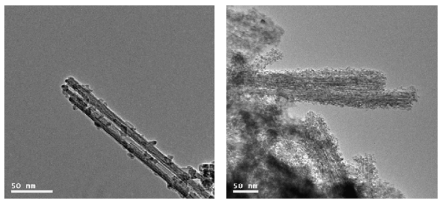

TiO_2 nanotubes-supported MS (TiO_2@MS, M = Cd, Zn) are synthesized by a simple wet chemical method at room temperature. The composites are active in the photooxidation reaction and their photocatalytic performances are enhanced compared with their corresponding MS nanoparticles or the support (TiO_2 nanotubes). The results indicate that the composites exhibit cooperative or synergetic effects of MS and the support (TiO_2 nanotubes), which greatly influences the optical and photocatalytic properties of the obtained TiO_2@MS composites.

Raman-spectroscopic investigation of Ba_2InTaO_6 and Sr_2InTaO_6 perovskites

A. Dias, L.A. Khalam, M.T. Sebastian and R.L. Moreira

Page 2143

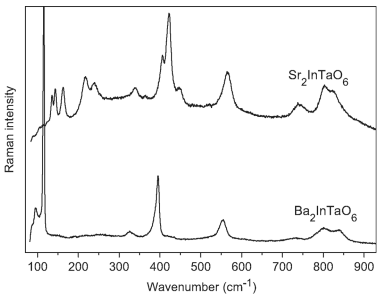

Raman analysis of Ba_2InTaO_6 and Sr_2InTaO_6 perovskites. Two different spectral profiles are clearly observed, which indicates that the ceramics likely to occur in different structures. Barium perovskites exhibit 14 Raman-active bands in a tetragonal structure, while strontium-based materials show 24 phonon modes associated with a lower-symmetry structure (monoclinic).

Synthesis and characterization of flower-like β-$Ni(OH)_2$ nanoarchitectures

Yuanyuan Luo, Guotao Duan and Guanghai Li

Page 2149

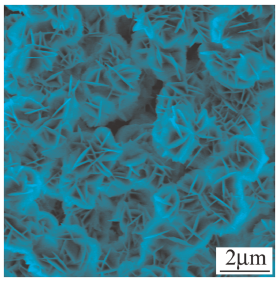

Flower-like $Ni(OH)_2$ nanoarchitectures were synthesized by a one-step mild hydrothermal reaction with the aid of ethylenediamine in $NiCl_2$ aqueous solution. The flower with the size of several micrometers in diameter is composed of the ultra-thin nanosheets of several nanometers in thickness. The flowers could be in catalysts, sensor and electrochromic devices, and alkaline rechargeable batteries.

Morphology-controlled nonaqueous synthesis of anisotropic lanthanum hydroxide nanoparticles

Igor Djerdj, Georg Garnweitner, Dang Sheng Su and Markus Niederberger

Page 2154

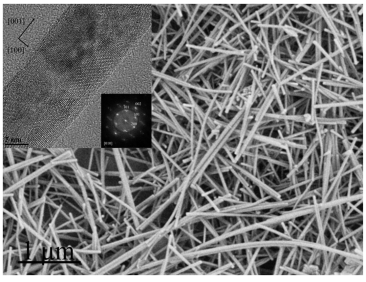

Lanthanum hydroxide nanoparticles are synthesized based on a nonaqueous sol-gel process involving the reaction of La(OiPr)$_3$ and $KMnO_4$ with organic solvents such as benzyl alcohol, 2-butanone and a 1:1 vol. mixture thereof. In dependence of the reaction parameters, the $La(OH)_3$ nanoparticles undergo a shape transformation from short nanorods to micron-sized nanofibers.

Syntheses, crystal structures, and optical properties of $K_3V_{0.32}Ta_{0.68}S_4$, $K_6Nb_{1.07}Ta_{2.93}S_{22}$, $K_6Nb_{2.97}Ta_{1.03}S_{25}$, $K_3Cu_3Nb_{0.98}Ta_{1.02}S_8$, and $KCu_2Nb_{0.53}Ta_{0.47}S_4$
Yuandong Wu and Wolfgang Bensch
Page 2166

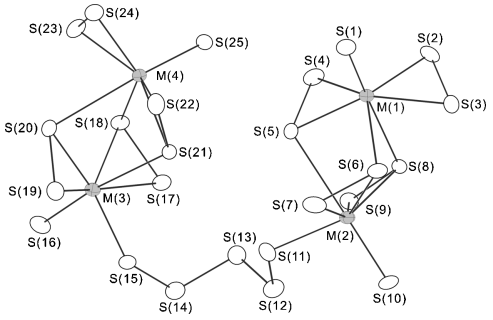

The five compounds $K_3V_{0.32}Ta_{0.68}S_4$, $K_6Nb_{1.07}Ta_{2.93}S_{22}$, $K_6Nb_{2.97}Ta_{1.03}S_{25}$, $K_3Cu_3Nb_{0.98}Ta_{1.02}S_8$, and $KCu_2Nb_{0.53}Ta_{0.47}S_4$ have been prepared in polychalcogenide melts. The structures of these compounds base on discrete tetrahedra $[MS_4]^{3-}$ (M = V/Ta), complex $[M_4S_{22}]^{6-}$ and $[M_4S_{25}]^{6-}$ anions comprised of two M_2S_{11} subunits bridged by a S_2 or S_3 chain, $^1_\infty[Cu_3M_2S_8]^{3-}$ anionic chains, and $^2_\infty[Cu_2MS_4]^-$ (M = Nb/Ta) anionic layers formed by corner sharing and edge sharing between CuS_4 and MS_4 tetrahedra.

^{17}O NMR studies of local structure and phase evolution for materials in the $Y_2Ti_2O_7$–$ZrTiO_4$ binary system
John L. Palumbo, Tobias A. Schaedler, Luming Peng, Carlos G. Levi and Clare P. Grey
Page 2175

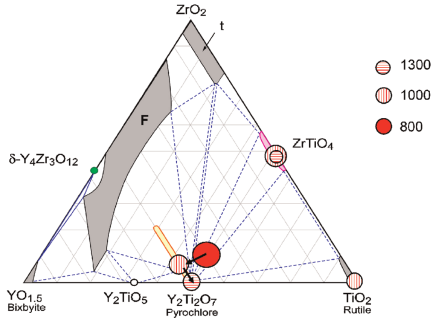

Schematic of the evolution of the crystalline phases in a material with stoichiometry $Y_{1.6}Zr_{0.4}Ti_2O_{7.2}$ (10Zr), as a function of heat treatment at 800, 1000 and 1300 °C.

Author inquiries

Submissions

For detailed instructions on the preparation of electronic artwork, consult the journal home page at http://authors.elsevier.com.

Other inquiries

Visit the journal home page (http://authors.elsevier.com) for the facility to track accepted articles and set up e-mail alerts to inform you of when an article's status has changed. The journal home page also provides detailed artwork guidelines, copyright information, frequently asked questions and more.

Contact details for questions arising after acceptance of an article, especially those relating to proofs, are provided after registration of an article for publication.

Language Polishing

Authors who require information about language editing and copyediting services pre- and post-submission should visit http://www.elsevier.com/wps/find/authorshome.authors/languagepolishing or contact authorsupport@elsevier.com for more information. Please note Elsevier neither endorses nor takes responsibility for any products, goods, or services offered by outside vendors through our services or in any advertising. For more information please refer to our Terms & Conditions at http://www.elsevier.com/wps/find/termsconditions.cws_home/termsconditions.

For a full and complete Guide for Authors, please refer to *J. Solid State Chem.,* Vol. 180, Issue 1, pp. *bmi–bmv*. The instructions can also be found at http://www.elsevier.com/wps/find/journaldescription.cws_home/622898/authorinstructions.

Journal of Solid State Chemistry has no page charges.